J. Fluid Mech. (2004), *vol.* 505, *pp.* 1–22. © 2004 Cambridge University Press
DOI: 10.1017/S0022112004008328 Printed in the United Kingdom

Elliptical instability in a rotating spheroid

By LAURENT LACAZE, PATRICE LE GAL AND STÉPHANE LE DIZÈS

Institut de Recherche sur les Phénomènes Hors Equilibre, UMR 6594, CNRS & Universités d'Aix-Marseille I et II, 49 rue F. Joliot-Curie, BP146, Technopole de Château-Gombert, 13384 Marseille Cédex 13, France

(Received 23 June 2003 and in revised form 2 December 2003)

This paper concerns the elliptical instability of a flow in a rotating deformed sphere. The aim of our work is to analyse the characteristics of this instability experimentally and to provide a theoretical model which accounts for the observations. For this purpose, an elastic and transparent hollow sphere has been moulded in a silicone gel block. The flow is visualized using Kalliroscope flakes illuminated with a laser sheet as the sphere is set into rotation and compressed by two rollers. The elliptical instability occurs by the appearance of the so-called 'spin-over' mode whose growth rate and saturation amplitude are measured by video image analysis at different Ekman numbers. Growth rates are predicted well by the linear stability analysis. A nonlinear model is developed and is shown to describe correctly the saturated regimes observed in the experiments. At low Ekman numbers, a secondary instability leading to an intermittent regime is also discovered.

1. Introduction

Our study is devoted to the appearance of the elliptical instability of a fluid flow contained in a rotating sphere. The elliptical instability is now a classical three-dimensional instability of fluid dynamics. It is known to affect and even to destroy vortical flows. As described in the review of Kerswell (2002), the instability mechanism lies on a resonance phenomenon between inertial (Kelvin) waves and external strain fields (Bayly 1986; Waleffe 1990). Therefore, characteristics of this instability could explain the three-dimensional undulations of strained vortices (Widnall, Bliss & Tsai 1974; Moore & Saffman 1975; Pierrehumbert 1986) observed in turbulence (Cadot, Douady & Couder 1995), in wakes (Leweke & Williamson 1998*b*), in vortex pairs (Leweke & Williamson 1998*a*; Meunier *et al.* 2002), or in rotating elliptical cylinders (Gledzer *et al.* 1975; Malkus 1989; Eloy, Le Gal & Dizès 2000). Another major interest of the elliptical instability, or its sister instability induced by precession (Noir, Jault & Cardin 2000), concerns the dynamics of the flows contained in rotating ellipsoids which are laboratory models of astrophysical objects subjected to tidal distortions induced by close gravitational bodies (Malkus 1968; Suess 1971; Gledzer & Ponomarev 1977; Kerswell 1994). More specifically, the occurrence of this instability in the motion of the molten iron cores of planets, such as the Earth, would be of prime importance in the understanding of the generation and of the dynamics of the magnetic fields of planets (Kerswell 1994; Kerswell & Malkus 1998). With this aim, Aldridge *et al.* (1997) have performed computations and built a rotating deformable shell where they observed some indications of the presence of the elliptical instability. In both cases (elliptical or precessional instability), we expect Kelvin waves to be excited. Note

https://doi.org/10.1017/S0022112004008328 Published online by Cambridge University Press

that, the dynamics of the Kelvin waves in this peculiar geometry (compared to the cylindrical or the spherical one) deserves its own mathematical treatment (Rieutord, Georgeot & Valdettaro 2001). Using the technique invented by Malkus (1989), and more recently used and extended to triangular distortions by Eloy, Le Gal & Dizès (2003), we have been able to apply an elliptical constraint to a deformable rotating sphere. The hollow sphere is moulded in a cylindrical block of transparent silicone gel. The cylinder is then placed in the device used by Eloy *et al.* (2000). It is set in rotation while it is gently compressed by two rollers positioned parallel to the rotation axis. A video camera records the motions of water seeded by Kalliroscope particles and illuminated by a laser sheet. The characteristics of the flow patterns are then measured by video image analysis and finally compared to the analytical results.

To our knowledge, this study presents for the first time, visualizations and measurements of the spin-over mode of the elliptic instability in a rotating sphere. The article is organized as follows. In § 2, we will recall and develop for some of its aspects, the mathematical description of the instability. Its linear and nonlinear analyses in a spherical geometry are presented. Then in § 3, experimental techniques and video image analysis are described and their results finally compared to our theoretical predictions.

2. Stability analysis of the flow

2.1. *Inertial waves in a sphere*

In this section, the main characteristics of the linear normal modes of the flow in a rotating sphere are recalled. Let us consider a sphere of radius R centred at the origin, rotating around a given axis (Oz) at the angular velocity Ω. In cylindrical coordinates, the basic flow velocity is given by $\boldsymbol{U} = r\Omega \boldsymbol{e}_\theta$ where r is the distance to the rotation axis and $\boldsymbol{e}_\theta$ the azimuthal unit vector. In the following, R and Ω will be used to normalize all spatial and time variables.

Let us perturb the velocity and pressure fields by a linear normal mode of azimuthal wavenumber m and frequency ω:

$$(\boldsymbol{u}', p') = (\boldsymbol{u}, p)\mathrm{e}^{\mathrm{i}(m\theta - \omega t)}.$$

In the non-viscous framework, the amplitude p of the perturbation pressure field is known to satisfy the so-called Poincaré equation (see for instance Greenspan 1968)

$$\frac{1}{r}\frac{\partial}{\partial r}\left(r\frac{\partial p}{\partial r}\right) - \frac{m^2}{r^2}p - \left(\frac{4}{\gamma^2} - 1\right)\frac{\partial^2 p}{\partial z^2} = 0, \tag{2.1}$$

with the following non-viscous boundary conditions

$$r\frac{\partial p}{\partial r} - \frac{2m}{\gamma}p - \left(\frac{4}{\gamma^2} - 1\right)z\frac{\partial p}{\partial z} = 0 \quad \text{at} \quad r^2 + z^2 = 1, \tag{2.2}$$

where $\gamma = \omega - m$ is the frequency of the perturbation in the rotating frame.

The solutions of this eigenvalue problem were given by Greenspan (1968). The viscous boundary-layer correction of these inviscid solutions is known to be singular at the critical latitude defined by $\gamma = -2\boldsymbol{n}\cdot\boldsymbol{z}$ where $\boldsymbol{n}$ is the sphere normal vector. In fact, this critical latitude generates boundary-layer eruptions in the main flow giving birth to shear layers in the core of the flow (Hollerbach & Kerswell 1995). It appears that for each m, there are a discrete number of eigenvalue families which are defined

https://doi.org/10.1017/S0022112004008328 Published online by Cambridge University Press

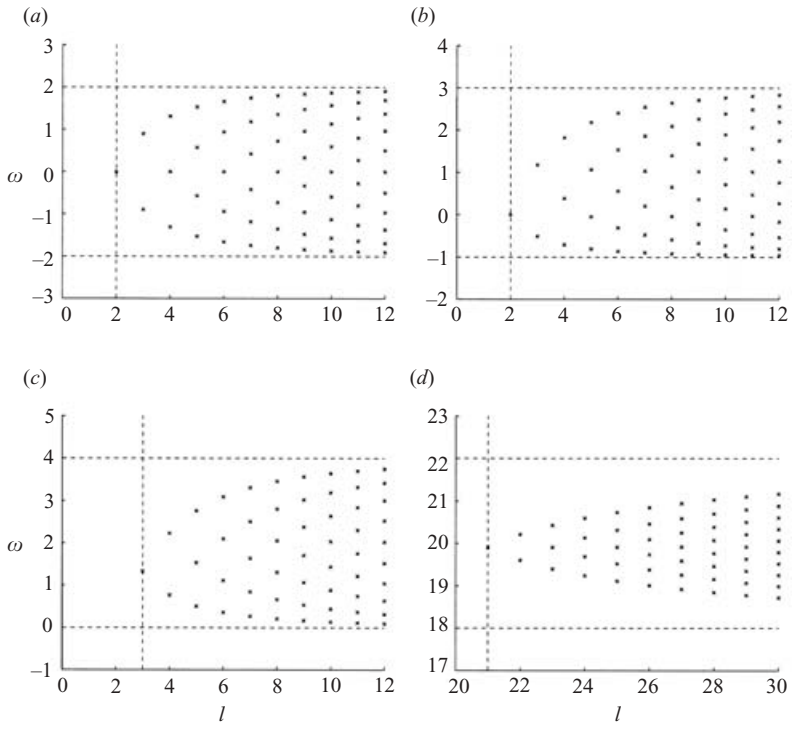


FIGURE 1. Eigenfrequencies versus l for (*a*) $m=0$, (*b*) $m=1$, (*c*) $m=2$, (*d*) $m=20$.

as the roots of the equation:

$$(1-x^2)\frac{\mathrm{d}\left(P_l^{|m|}(x)\right)}{\mathrm{d}x}+mP_l^{|m|}(x)=0; \qquad x=\tfrac{1}{2}\gamma, \tag{2.3}$$

where P_l^m is the Legendre polynomial of degree l and order m. These families are parameterized by the integers l and m. For each l and each m there are $l-m$ eigenvalues if $m\neq 0$ and $l-1$ eigenvalues if $m=0$. The eigenfunction associated with each eigenvalue γ is then given by the following expression:

$$p(r,z)=r^{|m|}z^e\prod_{j=1}^{N}\left(\xi_j^2\left(\xi_j^2-1\right)+\xi_j^2\left(1-\tfrac{1}{4}\gamma^2\right)r^2+\tfrac{1}{4}\gamma^2\left(1-\xi_j^2\right)z^2\right), \tag{2.4}$$

where $e=0$ if $(l-m)$ is even, and $e=1$ if $(l-m)$ is odd. The ξ_j, $j=1,\ldots,N$ are the zeros of P_l^m and the integer N is given by:

$$N=\tfrac{1}{2}(l-|m|) \quad \text{when} \quad l-|m| \quad \text{is even},$$
$$N=\tfrac{1}{2}(l-|m|-1) \quad \text{when} \quad l-|m| \quad \text{is odd}.$$

From these conditions, it appears that the frequencies ω are confined in the interval $m-2<\omega<m+2$. Moreover, for $m=0$, the frequency spectrum is symmetrical with respect to $\omega=m$. Note that this symmetry tends also to be recovered for large values of m.

The different examples displayed in figure 1 show the evolution of the frequency ω of the normal mode (Kelvin waves) as a function of the parameter l and for different azimuthal wavenumbers m. These graphs resemble a discrete version of the dispersion

https://doi.org/10.1017/S0022112004008328 Published online by Cambridge University Press

relation of the non-viscous modes calculated in a rotating cylinder where l is replaced by the axial wavenumber of the mode (see Eloy 2000, for instance). An equivalent spatial wavenumber can be defined here as $l-m$. In particular, the larger $l-m$ is, the more complex is the spatial structure of the eigenmode.

When viscous effects are taken into account, the normal modes are damped. *A priori*, two sources of damping have to be considered: the volume viscous damping ν_V which is proportional to the Ekman number $E=\nu/\Omega R^2$ and the surface viscous damping ν_S proportional to $\sqrt{E}$ which is induced by the boundary layers and the internal singular shear layers. Generally, volume effects become large when the radial wavenumber increases, but in the special case of the sphere, volume viscous damping exactly vanishes for any inertial mode (see Zhang *et al.* 2001). This implies that for the present flow, viscous damping can only be due to surface effects, that is internal shear layers and boundary layers. The viscous damping associated with internal shear layers is difficult to calculate. It is expected to be small compared to the contribution from boundary layers for the unstable modes we shall consider (see Hollerbach & Kerswell 1995). It will not be considered in the present study.

2.2. *Elliptical instability*

2.2.1. *Linear stability theory*

Consider now that the sphere is slightly elliptically deformed such that the radial and azimuthal components of the basic velocity field become:

$$U=\varepsilon r\sin(2\theta),$$
$$V=r+\varepsilon r\cos(2\theta).$$

Here, it is implicitly assumed that the small strain rate ε induced by the sphere deformation is uniform in the whole flow. This small strain field added on the rotating flow is the source of the elliptical instability. As explained by many authors (see Kerswell 2002, for a review), the basic mechanism is the resonant coupling of two eigenmodes of the underlying rotating flow with the strain field. The condition of perfect resonance corresponds to the existence of two normal modes of identical frequency and azimuthal wavenumbers m and $m+2$. For a Rankine vortex, Eloy & Le Dizès (2001) showed that this condition of resonance always leads to instability. However, they also demonstrated that the instability growth rate was strongly dependent on the spatial coherence of the resonant modes. In particular, they showed that principal resonant configurations, associated with the crossing of branches of the dispersion relation with the same label, provided an unstable growth rate two orders of magnitude larger than the others. In a sphere, as mentioned above, continuous branches become points. This implies that perfect resonance is exceptional. In order to provide instability conditions for small but finite strain field it is therefore necessary to consider also imperfect resonance. This means that we allow a small frequency detuning $\delta\omega$ between two 'resonant' modes. Based on the results for the Rankine vortex, we shall also focus on principal configurations, that is couples of modes m and $m+2$ with the same l and same root label in equation (2.3). This hypothesis is also justified by Kerswell (1993) who showed that no instability is possible if the two modes do not have the same l.

Figure 2 displays the frequencies of the modes for $m=1$ and $m=-1$ ($\circ$ and $\times$, respectively). Note that there exists only one single perfect resonant configuration ($\diamond$). This perfect resonance is associated with a particular symmetry $m\rightarrow -m$ and occurs for $l=2$. No similar perfect resonance is obtained for other couples of azimuthal wavenumber $(m, m+2)$. The large characters in figure 2 indicate the principal

https://doi.org/10.1017/S0022112004008328 Published online by Cambridge University Press

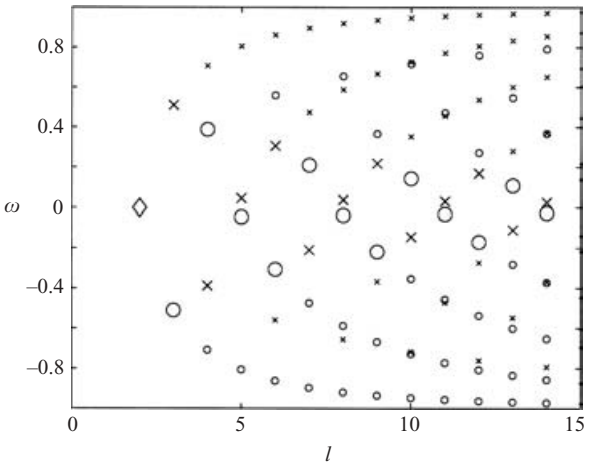


FIGURE 2. Eigenfrequencies for ○, $m=1$ and ×, $m=-1$. Large symbols represent principal configurations of quasi-resonant modes. The spin-over mode indicated by ◇ corresponds to a perfect resonance.

configurations as l varies (a large ○ and a large × for each configuration). Note that the frequency detuning between the two modes of these principal configurations is important for small l (except for $l=2$), but it decreases and tends to zero as l increases. The stabilizing effect of the frequency detuning is therefore expected to go to zero for large l. A viscous surface damping of $O(\sqrt{E})$ is, however, expected to be present always in this limit. The largest non-viscous growth rate associated with a perfect resonance is of order ε. Detuning and viscosity could therefore overcome the instability when $\delta\omega \geqslant O(\varepsilon)$ and $E \geqslant O(\varepsilon^2)$. If a perturbation analysis is done for small ε using these scalings, the leading-order growth rate including detuning and viscous effects can be obtained. Such an analysis has been performed for various configurations (see Tsai & Widnall (1976) or Eloy & Le Dizès (2001) for a Rankine vortex and Kerswell (1994) for a rotating spheroid). The final result is an equation for the growth rate $\sigma=\sigma_1\varepsilon$ of two coupled resonant normal modes:

$$\left(\sigma_1+\mathrm{i}\delta\omega/\varepsilon-\mathrm{i}\sqrt{E}/2\varepsilon\left(\delta\omega_s^1-\delta\omega_s^2\right)-\sqrt{E}\nu_s^1/\varepsilon\right)$$
$$\times\left(\sigma_1-\mathrm{i}\delta\omega/\varepsilon+\mathrm{i}\sqrt{E}/2\varepsilon\left(\delta\omega_s^1-\delta\omega_s^2\right)-\sqrt{E}\nu_s^2/\varepsilon\right)=\zeta^2. \quad (2.5)$$

In this equation, $\delta\omega_s^1$ and ν_s^1 (respectively $\delta\omega_s^2$ and ν_s^2) are frequency and damping rate corrections induced by surface viscous effects on the first mode (respectively on the second mode). The coefficient ζ is the 'coupling term' which generates the instability. It provides the maximum growth rate of the instability if both detuning and viscous damping are negligible. In figures 3 and 4, the coefficient ζ is plotted for several quasi-resonant configurations as a function of the label l. In figure 3, only the principal configurations $(-1, 1)$ shown on figure 2 are considered. In figure 4, the coupling term is computed for principal configurations of different azimuthal wavenumbers but only configurations satisfying $\delta\omega\leqslant 0.1$ are kept. On both figures, the dashed line indicates the value 9/16 obtained for the growth rate of the instability for inviscid and unbounded flows (Waleffe 1990). Figure 3 demonstrates that ζ can be well above 9/16. This, however, concerns only the strongly detuned configurations ($l=3$, 4 and 6). For weakly detuned configurations (figure 4), the largest value of

https://doi.org/10.1017/S0022112004008328 Published online by Cambridge University Press

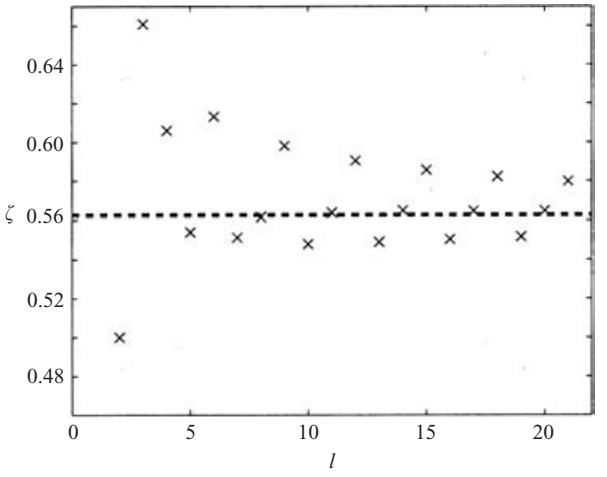


FIGURE 3. Coupling coefficient ζ for the principal configurations shown on figure 2: $(m_1, m_2) = (-1, 1)$.

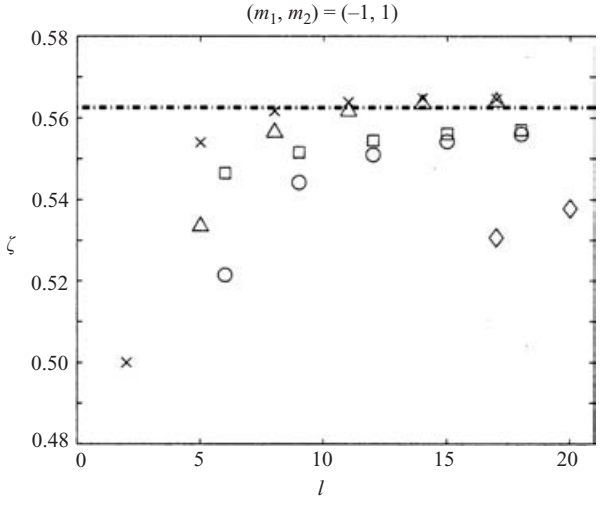


FIGURE 4. Coupling coefficient ζ for principal configurations satisfying $\delta\omega \leqslant 0.1$. ×, $(m_1, m_2) = (-1, 1)$; □, $(m_1, m_2) = (0, 2)$; △, $(m_1, m_2) = (1, 3)$; ○, $(m_1, m_2) = (2, 4)$; ◇, $(m_1, m_2) = (8, 10)$.

ζ is close to 9/16. Figure 4 also shows that for a fixed l, the largest value of ζ is always reached for a configuration $(-1, 1)$. This anticipates the predominance of $(-1, 1)$ modes that will be observed below.

For the perfectly resonant configuration between modes $m = 1$ and $m = -1$, pointed out on figure 2 at $l = 2$, the non-viscous growth rate can be calculated analytically: $\sigma_1 = 1/2$ (× for $l = 2$ in figures 3 and 4). This configuration is stationary and corresponds to a solid-body rotation around an axis perpendicular to the main rotation axis (Oz). It is called the spin-over mode. It plays a particular role, as shown below.

https://doi.org/10.1017/S0022112004008328 Published online by Cambridge University Press

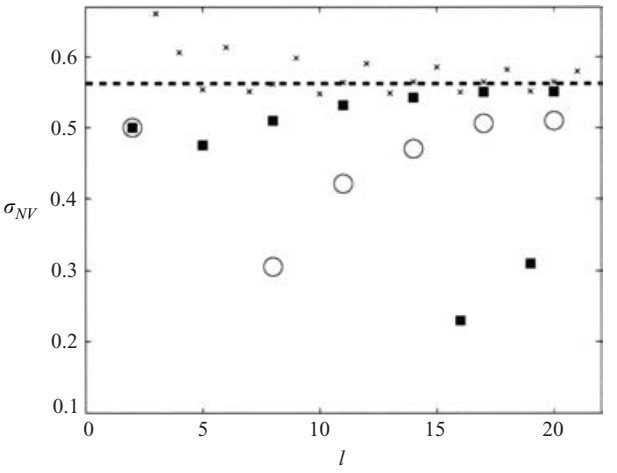


FIGURE 5. Non-viscous growth rate of the principal configurations $(m_1, m_2) = (-1, 1)$. ○, $\varepsilon = 0.08$; ■, $\varepsilon = 0.16$. The coupling coefficient ζ is reported from figure 3 (×).

As soon as $\delta\omega$ is non-zero, the non viscous growth rate σ_{NV}/ε depends on the strain rate ε (see equation (2.5)):

$$\frac{\sigma_{NV}}{\varepsilon} = \sqrt{\zeta^2 - \frac{\delta\omega^2}{\varepsilon^2}}.$$

The non-viscous growth rate, however, remains always smaller than the 'coupling term' ζ because of detuning. Figure 5 shows the evolution of the non-viscous growth rate of the most unstable principal configurations $(-1, 1)$ for the two values of ε that will be used later in the experiment. Note that the detuning effect is clearly visible for the smallest value of ε ($\varepsilon = 0.08$). For this value, we require $l \geqslant 17$ to obtain another $(-1, 1)$ configuration more unstable than the spin-over mode (first mode $l = 2$). If we consider other types of principal configuration $[(m_1, m_2) \neq (-1, 1)]$, we have to go to even higher values of l, because the non-viscous growth rate of such configurations is smaller as expected from the values of ζ (figure 4) and larger values of the detuning.

Surface viscous effects damp the normal modes but also change their frequency. Concerning the elliptical instability, the frequency change can be destabilizing if it tends to decrease the detuning of two quasi-resonant modes. This has been observed for a few configurations. However, it has always been found to be smaller than the damping part.

In figure 6, the viscous growth rate of the most unstable principal configurations $(-1, 1)$ are plotted for different Ekman numbers and two values of ε. Only the surface contribution due to the boundary layers is computed. As mentioned above, the part coming from internal shear layers is not considered. Hollerbach & Kerswell (1995) demonstrated that this contribution is negligible for the spin-over mode. We assume here that it is also the case for the other modes. Figure 6 shows that the spin-over mode is the most unstable configuration $(-1, 1)$ in both cases $\varepsilon = 0.08$ and $\varepsilon = 0.16$ for all Ekman numbers $E \geqslant 5 \times 10^{-5}$. The importance of this mode for large Ekman numbers is also visible on figure 7 on which are reported the characteristics of the most unstable configuration in the (ε, E^{-1})-plane. This figure demonstrates that the

https://doi.org/10.1017/S0022112004008328 Published online by Cambridge University Press

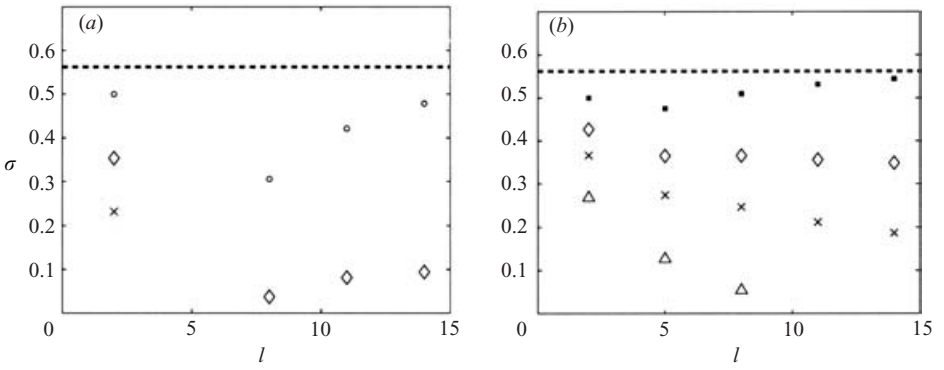


FIGURE 6. Viscous growth rates for the principal configurations $(-1, 1)$ for (a) $\varepsilon = 0.08$ and (b) $\varepsilon = 0.16$. (○, ■), $E = 0$; △, $E = 2 \times 10^{-4}$; ×, $E = 6.5 \times 10^{-5}$; ◇, $E = 5 \times 10^{-5}$.

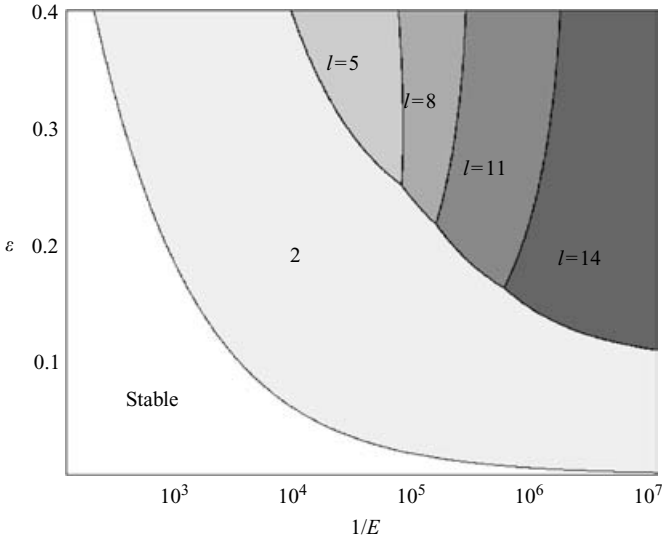


FIGURE 7. Most unstable mode as a function of E and ε. All the most unstable modes are principal configurations with azimuthal wavenumbers $(-1, 1)$. Only the value of l changes, as indicated. The spin-over mode corresponds to $l = 2$.

spin-over mode is the first mode to be destabilized as either ε or $1/E$ is increased. However, as noted above, the spin-over mode is not always the most unstable mode. For a fixed deformation ε (not too small), the characteristics of the most unstable mode change as $1/E$ increases. The most unstable mode remains a principal configuration $(-1, 1)$, but its spatial structure becomes more and more complex because l increases. An illustration of such a complex mode is provided in figure 8. Note also that for the Ekman numbers considered in figure 7, the spin-over mode is always the first mode to be destabilized as ε increases. However, this may not be the case for very small Ekman numbers, as in those encountered in astrophysical situations. An asymptotical study in the limit of small Ekman numbers could be useful to solve this issue.

https://doi.org/10.1017/S0022112004008328 Published online by Cambridge University Press

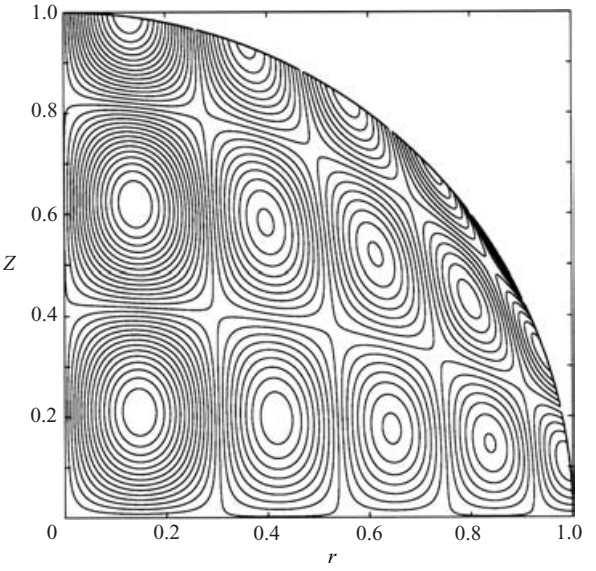


FIGURE 8. Illustration of the complex spatial structure of some of the most unstable modes. The (first) principal configuration $(-1, 1)$ for $l = 14$. Here are displayed the isocontours of the pressure amplitude in the transverse (r, z)-plane.

For the parameters of the experiments described in § 3, the spin-over mode is always the most unstable configuration. Its growth rate, calculated from equation (2.5), is

$$\sigma = \varepsilon\sqrt{0.5^2 - (0.259)^2\frac{E}{\varepsilon^2}} - 2.62\sqrt{E}. \tag{2.6}$$

If we do not consider the boundary-layer flow, the spatial structure of the spin-over mode is particularly simple as it is a solid-body rotation around an axis in a plane perpendicular to the (Oz) axis. It is convenient to define the orientation angle ϕ of this axis in that plane. This permits us to write the velocity and vorticity fields of this flow as

$$\begin{aligned} \boldsymbol{u} &= A(t)\begin{vmatrix} z\sin(\phi) \\ z\cos(\phi) \\ r\sin(\phi) \end{vmatrix} \\ \omega = \frac{1}{2}\begin{vmatrix} \Omega_1 \\ \Omega_2 \\ 0 \end{vmatrix} &= A(t)\begin{vmatrix} \cos(\phi) \\ \sin(\phi) \\ 0 \end{vmatrix} \end{aligned} \tag{2.7}$$

where $A(t)$ is the amplitude of the spin-over mode. In the linear regime $A(t)$ evolves as $\mathrm{e}^{\sigma t}$ with $\sigma \sim \varepsilon/2$ and ϕ remains constant. This behaviour is modified by nonlinearity as presented in the next section.

2.3. *Nonlinear evolution of the spin-over mode*

The simple form of the spin-over mode permits the construction of a nonlinear model. Hough (1895) and Poincaré (1910) were the first to our knowledge to give the fully nonlinear system of equations describing non-viscous solid-body rotation in a spheroid. More recently, Gledzer & Ponomarev (1977) and Biello, Saldanha &

https://doi.org/10.1017/S0022112004008328 Published online by Cambridge University Press

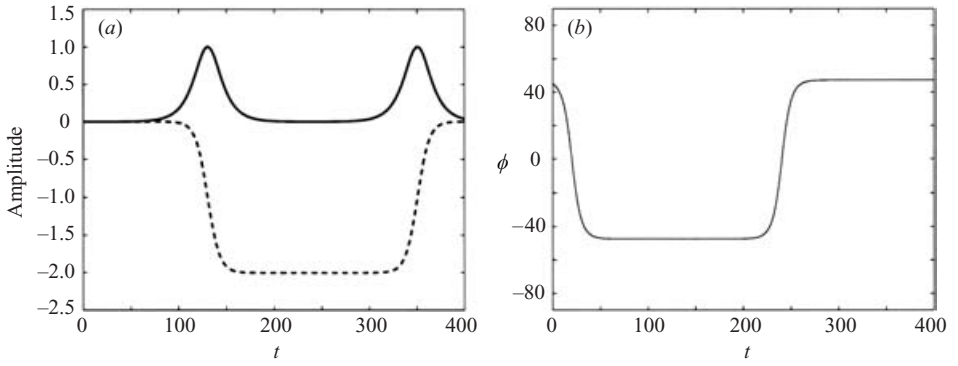


FIGURE 9. Nonlinear inviscid evolution of the spin-over mode. (*a*) ——, amplitude A of the spin-over mode; - - -, nonlinear correction Ω_3. (*b*) Phase ϕ of the spin-over mode.

Lebovitz (2000), continued this study. Their system, with our notation, reduces to:

$$\left.\begin{aligned}(2-\varepsilon)\dot{\Omega}_1 &= -\varepsilon(1+\Omega_3)\Omega_2,\\ (2+\varepsilon)\dot{\Omega}_2 &= -\varepsilon(1+\Omega_3)\Omega_1,\\ \dot{\Omega}_3 &= \varepsilon\Omega_1\Omega_2,\end{aligned}\right\} \tag{2.8}$$

where $(\Omega_1, \Omega_2, \Omega_3)$ are the rotation intensity around major, minor and z-axes. The rotation velocities Ω_1 and Ω_2 are the components of the spin-over mode vorticity as seen before. Ω_3 comes from the nonlinear feedback of the spin-over mode on the basic rotation around the z-axis. If we write $\Omega_\perp = \Omega_1 + \mathrm{i}\Omega_2 = A\mathrm{e}^{\mathrm{i}\phi}$, the amplitude A is the amplitude of the spin-over mode and ϕ is, as before, the orientation of its vorticity in the equatorial plane (see (2.7)). In particular, when $\phi = \pi/4$, the vorticity is aligned along with the principal direction of stretching and thus is subject to strong amplification. From (2.8), we obtain a single equation for $\Omega_\perp$ which reads (see Kerswell 2002):

$$\dot{\Omega}_\perp = -\tfrac{1}{2}\mathrm{i}\varepsilon\bar{\Omega}_\perp + O(\varepsilon^2|\Omega_\perp|, \varepsilon|\Omega_\perp|^3),$$

where $\bar{\Omega}_\perp$ is the complex conjugate of $\Omega_\perp$. As expected, (2.9) shows that the spin-over mode growth rate is equal to 1/2. Note that contrary to the case of the elliptical instability in a cylinder (Eloy *et al.* 2000, 2003), the contribution from the nonlinear terms here remains small as long as the amplitudes are not of order 1. This implies that in the non-viscous case, the linear regime is expected to be valid up to large amplitudes even in the limit of small ε.

The non-viscous time evolution of $\Omega_\perp$ and Ω_3 is computed from (2.8) and is illustrated in figure 9. It appears that Ω_3 can be smaller than -1 which means that the axial rotation changes its sign. When such an event occurs (at $t = 140$ in the figure), the stretching direction becomes a direction of compression which induces in turn a decrease of the amplitude of the spin-over mode. Thus, the system enters a cycle of heteroclinic oscillations. Although this singular dynamic is very attractive, it is not expected to resist the addition of a small amount of viscous damping generated in the boundary layers. As no rigorous viscous nonlinear theory of the dynamic of the spin-over mode is accessible today, we propose here to consider a simple model where only the viscous effects associated with the boundary layers are taken into account. Indeed, as already mentioned the global volume viscous effects are exactly null and the contribution of the internal shear layers is expected to be small. This model is

https://doi.org/10.1017/S0022112004008328 Published online by Cambridge University Press

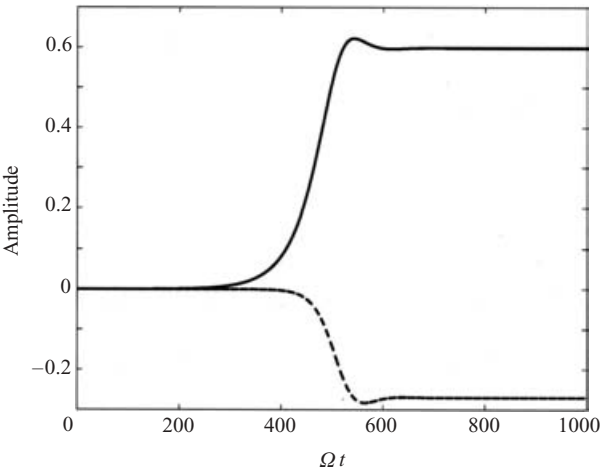


FIGURE 10. Nonlinear viscous evolution of the spin-over mode amplitude (solid line) and of the nonlinear correction Ω_3 (dashed line) for $E = 5 \times 10^{-4}$, $\varepsilon = 0.16$.

written as:

$$\dot{\Omega}_1 = -\frac{\varepsilon}{(2-\varepsilon)}(1+\Omega_3)\Omega_2 + \nu_{SO}\Omega_1, \tag{2.9a}$$

$$\dot{\Omega}_2 = -\frac{\varepsilon}{(2+\varepsilon)}(1+\Omega_3)\Omega_1 + \nu_{SO}\Omega_2, \tag{2.9b}$$

$$\dot{\Omega}_3 = \varepsilon\Omega_1\Omega_2 + \nu_{EC}\Omega_3 + \nu_{NL}\left(\Omega_1^2 + \Omega_2^2\right). \tag{2.9c}$$

In these equations, $\nu_{SO} = -2.62\sqrt{E}$ is the linear viscous damping rate of the spin-over mode given in (2.6) and first calculated by Greenspan. The coefficient $\nu_{EC} = -2.85\sqrt{E}$ in (2.9*c*) is the linear viscous damping of axial rotation. The third coefficient $\nu_{NL} = 1.42\sqrt{E}$ is the viscous boundary-layer effect on the nonlinear interaction of the spin-over mode with itself. It is calculated in the same way as the others (see Greenspan 1968). It is important to mention that the equations do not contain all the viscous terms of $O(\sqrt{E})$. Interactions of the viscous nonlinear correction with the spin-over mode have not been considered. Moreover, we recall that the nonlinear corrections induced by the internal shear layers have also been neglected. System (2.9) generates a dynamic which is significantly different from the non-viscous evolution (figure 9). In particular, the oscillations disappear. Figure 10 shows a typical evolution for $\varepsilon = 0.16$ and $E = 5 \times 10^{-4}$. Both the amplitude A and the nonlinear correction Ω_3 now saturate. As we will see in the next section, this type of evolution is in agreement with the experimental observations.

3. Experimental results

3.1. *Experimental set-up*

The experimental set-up is presented on figure 11. The device consists essentially of that used by Eloy *et al.* (2003) in their study of the elliptical instability in the cylindrical geometry. The main idea, originally exploited by Malkus (1989) is to set in rotation a flexible container whose boundary is deformed by a gentle compression created by two rollers. These rollers are positioned on each side of the container in such a way that its cross-section has an elliptic shape. In this way, the streamlines

https://doi.org/10.1017/S0022112004008328 Published online by Cambridge University Press

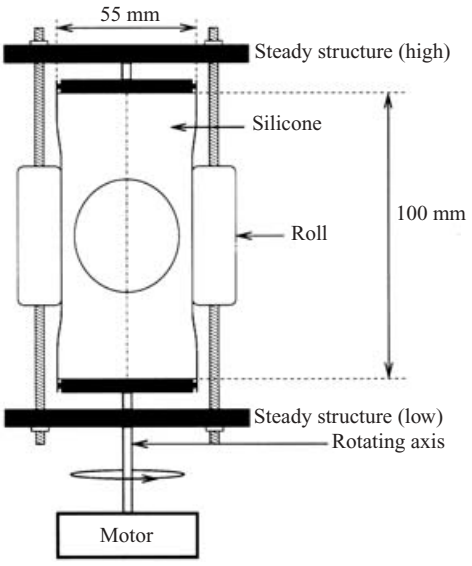


FIGURE 11. Experimental set-up.

of the rotating flow are closed ellipses and as the boundary rotates together with the fluid, eventual centrifugal instabilities are suppressed.

The hollow sphere is realized with the help of a ping-pong ball. This ball is plunged into a cylinder filled with silicone polymer (NUSIL-MED 6015) which is then cured at a temperature of 60 °C. This silicone gel is optically transparent and thus permits visualizations and non-intrusive measurements of the flow. The ball, made of cellulose nitrate is then dissolved in a solvent (ethyl acetate) which is injected inside the ball by two 2 mm stainless steel pipes aligned on the axis of the silicone cylinder. These pipes will also be used to fill up the sphere with the working fluid (water at room temperature). Moreover, during the moulding operations, these pipes hold the ping-pong ball firmly in place inside the gel cylinder. The hollow sphere obtained has a radius of 21.75 mm and is centred inside the transparent silicone cylindrical block whose diameter is 50 mm and length is 100 mm. This cylinder is then clamped on the rotating device and compressed by the use of two rollers. Therefore, the radius of the sphere reads as required in the previous section:

$$R(\theta, z) = (1 - z^2)^{1/2}\left(1 - \tfrac{1}{2}\varepsilon \cos(2\theta)\right).$$

The angular velocity of the sphere is varied between 0 and 300 r.p.m. by an a.c. electric motor which is controlled with an accuracy better than 2%. The range of Ekman numbers which is explored is $[6.5 \times 10^{-5}, 10^{-1}]$. The ellipticity of the container is determined by the separation distance between the rollers and cannot be changed during rotation. Two values of ε have been chosen: 0.08 and 0.16. When the rotation rate of the spheroid is fixed to the desired value, the container is stopped and a delay time of several minutes is necessary to damp any flows before starting the rotation again. Each run consists of a spin-up regime during which water is set in rotation. Then, if the rotation rate is large enough, the development of the instability can be observed. As the experiments are realized near the instability threshold, the characteristic growth time of the instability is much larger than the transient time of the spin-up and decorrelation of both phenomena is expected.

https://doi.org/10.1017/S0022112004008328 Published online by Cambridge University Press

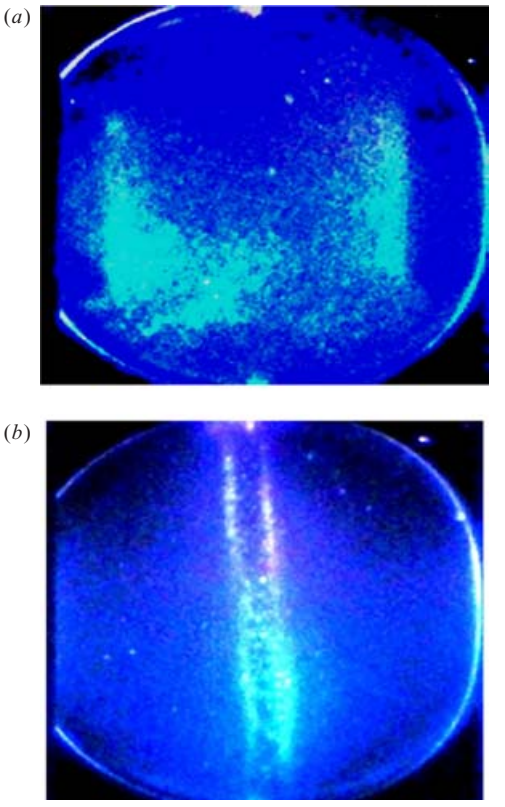


FIGURE 12. Two snapshots in a meridional plane of the spin-up in the ellipsoid for $E = 2.5 \times 10^{-4}$ and $\varepsilon = 0.16$. The progression of the front is observed at (*a*) the beginning and (*b*) the end of the spin-up phase.

The flow is seeded with anisotropic particles (Kalliroscope) and a thin light sheet formed using a 4 W argon laser, is sent on a meridional plane of the flow. The particles reflect the light following their orientation and thus permit the observation of the flow patterns. As presented in figure 12(*a*), the spin-up shear layer progresses toward the axes of rotation. At the end of this transient, the vortex core is particularly well visualized (see figure 12*b*). This transient lasts around 10 s in the range of Ekman numbers that we explore.

3.2. *Visualization of the instability*

Figure 13 shows an asymptotic state reached some minutes after the onset of rotation. The stationary S shape of the vortex core reflects the combination of the basic driving rotation versus the vertical axis, with the solid-body rotation around an axis contained in the horizontal plane and due to the spin-over mode. This mode is very strong near the centre of the sphere and its magnitude decreases closer to the boundary. In particular, the vortex core reconnects to the rotation axis at the poles of the sphere. In the following section, we present the video analysis of these visualizations that permits the extraction of the growth rate of the instability and also the description of the saturated state.

Another way to observe the flow is to send the laser sheet in a plane perpendicular to the axis of rotation. The flow is now observed from above. Figure 14 presents such

https://doi.org/10.1017/S0022112004008328 Published online by Cambridge University Press

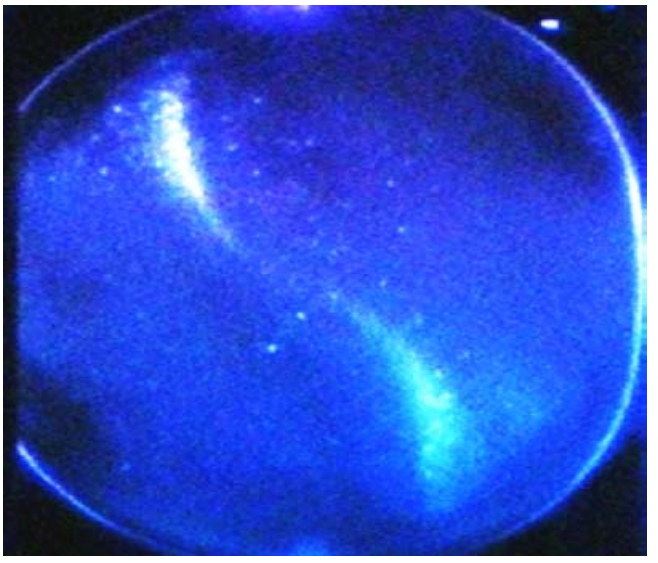


FIGURE 13. Visualization of the spin-over mode in a meridional plane for $E = 2.5 \times 10^{-4}$ and $\varepsilon = 0.16$. The typical S shape of the rotation axis is due to the combination of the main rotation, the spin-over mode and viscous boundary layers.

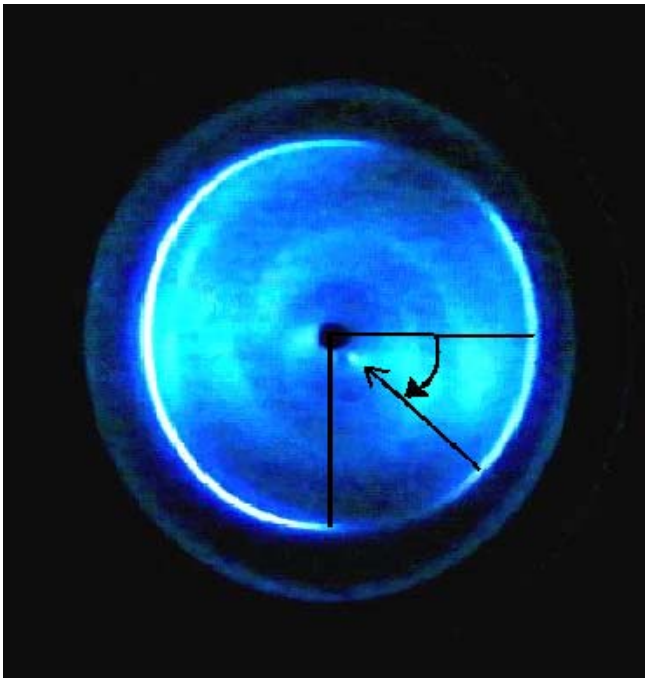


FIGURE 14. Visualization of the spin-over mode in a plane perpendicular to the main rotation axis for $E = 2.9 \times 10^{-4}$ and $\varepsilon = 0.16$. The bright spot, indicated by the arrow, is the rotation centre in the visualization plane. It is approximatively oriented along with the principal direction of stretching, that is $\pi/4$ away from the ellipse axis as indicated.

https://doi.org/10.1017/S0022112004008328 Published online by Cambridge University Press

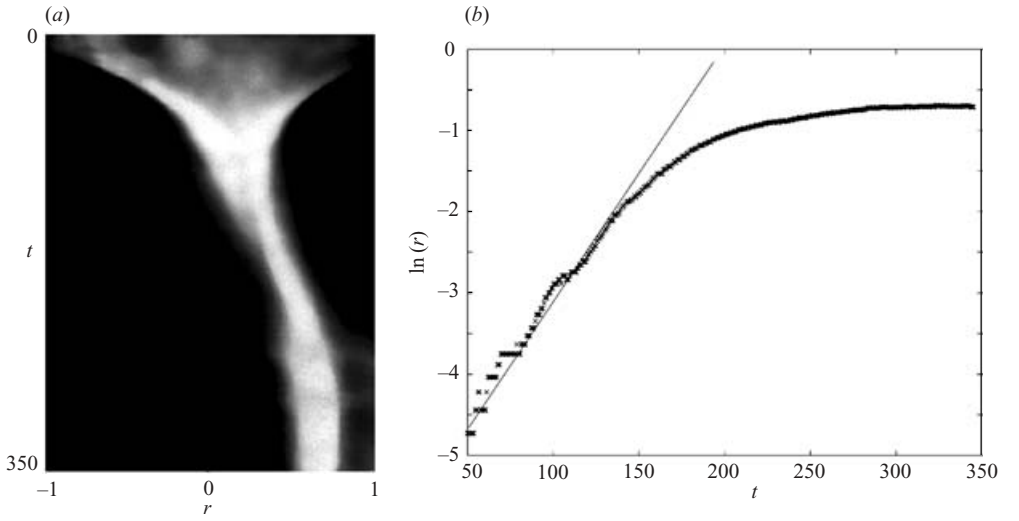


FIGURE 15. (*a*) Spatio-temporal evolution of the flow recorded along a line oriented along with the principal direction of stretching. The spin-up phase, characterized by the convergence of the two fronts towards the centre, and the growth of the spin-over mode, characterized by the displacement of the vortex centre position, are both visible. (*b*) Semilogarithmic plot of the vortex centre position as a function of time. The exponential growth and the saturation are well defined. ($E = 2.5 \times 10^{-4}$ and $\varepsilon = 0.16$).

a visualization in a plane near the maximum of distortion of the S shaped vortex core. The rollers, not visible on this image, are positioned on each side of the sphere, on the horizontal axis of the figure. As can be clearly observed, the vortex core intersects the plane of visualization and a bright spot is visible. In fact the whole flow rotates around this spot which is clearly off-centred and aligned in a direction close to the direction of maximum stretching, at $\pi/4$ from the ellipse axes.

Figures 13 and 14 agree with the deformation of the vortex core as predicted by the theoretical analysis presented in the previous sections. This mode is observed and saturates above a critical Ekman number which depends on the ellipticity ε (theoretically $E_c = 2.31 \times 10^{-4}$ for $\varepsilon = 0.08$ and $E_c = 9.23 \times 10^{-4}$ for $\varepsilon = 0.16$). Below a secondary threshold (around $E = 2 \times 10^{-4}$ for $\varepsilon = 0.16$), high-frequency small-scale structures appear between the vortex core and the sphere surface. At $E = 1.68 \times 10^{-4}$, a secondary instability destabilizes the spin-over mode and an intermittent regime appears. Finally, at higher rotation rate, a permanent disordered flow occurs in the spheroid.

3.3. *Video analysis of the instability near threshold*

The spatio-temporal diagram shown in figure 15(*a*) represents the time evolution of the light intensity recorded on a horizontal chord in a meridional plane chosen so that the vortex core is clearly visible, as can be seen in figure 13. The chord is positioned 5 mm under the equatorial plane. After the spin-up transient which is represented by the funnel shape of the bright area, the growth of the mode amplitude is directly linked to the deviation of this bright area from the axis of symmetry of the figure as time increases. As expected, the two phenomena (spin-up and spin-over) are well separated in time. Then the simple shape of the spin-over mode permits us to estimate quantitatively the growth rate of the instability. Indeed, we know that the

https://doi.org/10.1017/S0022112004008328 Published online by Cambridge University Press

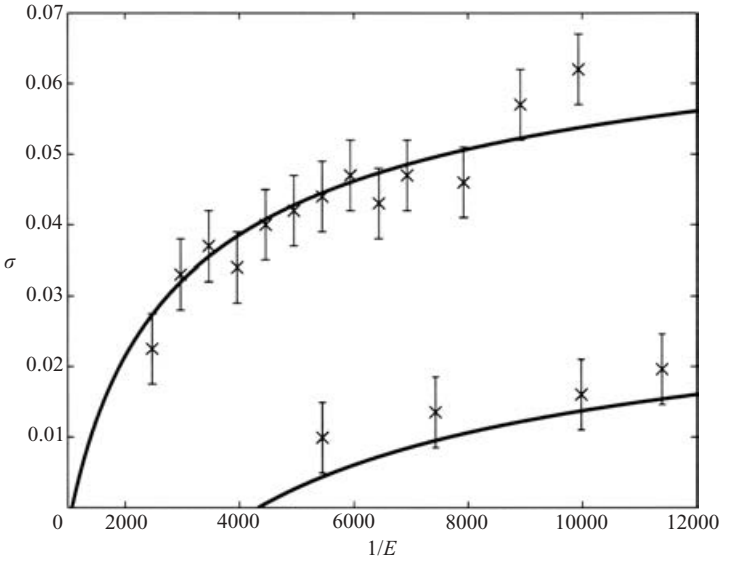


FIGURE 16. Growth rate versus the inverse of the Ekman number for $\varepsilon = 0.08$ (lower) and $\varepsilon = 0.16$ (upper). Experimental results ($\times$) and linear theory (solid line).

total velocity can be written as $v(r, z) = r\boldsymbol{e}_\theta \pm A(t)\,(z\sin(\theta)\boldsymbol{e}_r + z\cos(\theta)\boldsymbol{e}_\theta - r\sin(\theta)\boldsymbol{e}_z)$. As the plane of visualization was chosen so that $\theta = 0$ or π, the velocity is purely azimuthal and the core vortex position (vanishing velocity) is defined by $r = \pm A(t)z$. As z is equal to a constant, given by the position of the chosen chord, the temporal evolution of r gives exactly the temporal growth of the instability. Figure 15(b) shows the deformation of the vortex core versus time in semi-logarithmic scale. As it can be seen on this figure, the exponential growth is perfectly recovered before saturation.

Using this video image analysis, we are able to measure the experimental growth rate for different Ekman numbers. Figure 16 shows the comparison between the experimental values measured for two values of ε and the corresponding theoretical prediction computed as shown in § 2. As observed, the comparison between the experimental and theoretical growth rates is good, specially for $\varepsilon = 0.16$. In particular, the calculated threshold values ($E_c = 2.31 \times 10^{-4}$ for $\varepsilon = 0.08$ and $E_c = 9.23 \times 10^{-4}$ for $\varepsilon = 0.16$) are consistent with the experimental observations. The error bars are estimated from the standard deviation which is obtained from different experimental runs. The errors come from the difficulty in acurately determining the position of the rotation axis in the spatio-temporal diagrams.

The comparison of these experimental results with the nonlinear model predictions can also be investigated. Figure 17 shows the time evolutions of the amplitude of the vortex core deformation for two chosen Ekman numbers. As can be seen, results compare correctly although our experimental measurements do not show the overshoot fluctuations occurring just after the initial exponential growth. As observed in figure 17, the theoretical saturation of the amplitude is reached after some damped oscillations. This feature was not observed in the experiment. Note, however, that the estimation of the asymptotic amplitude of deformation is correctly recovered just above threshold but remains close to the values found theoretically at the overshoot. Indeed, this phenomenon is confirmed by the comparison of the saturation angle versus z of the vortex core deformation as a function of the Ekman number.

https://doi.org/10.1017/S0022112004008328 Published online by Cambridge University Press

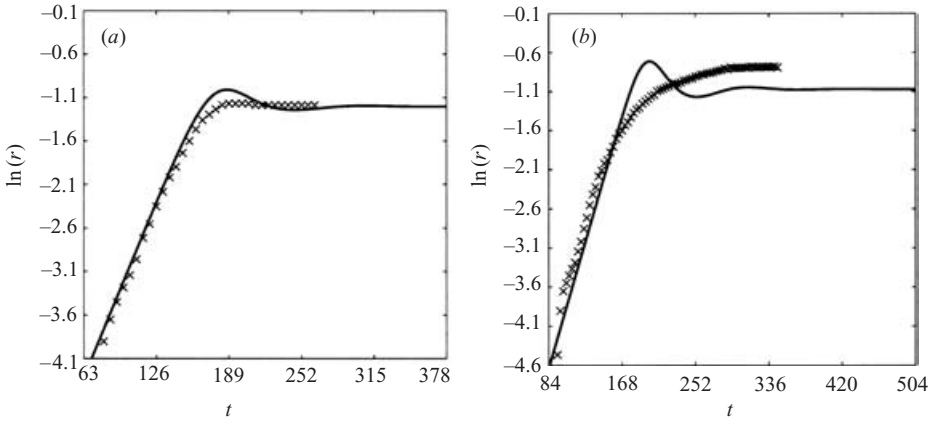


FIGURE 17. Comparison between the experimental results (×) and the nonlinear model for (*a*) $E = 3.4 \times 10^{-4}$ and (*b*) $E = 2.5 \times 10^{-4}$ with $\varepsilon = 0.16$.

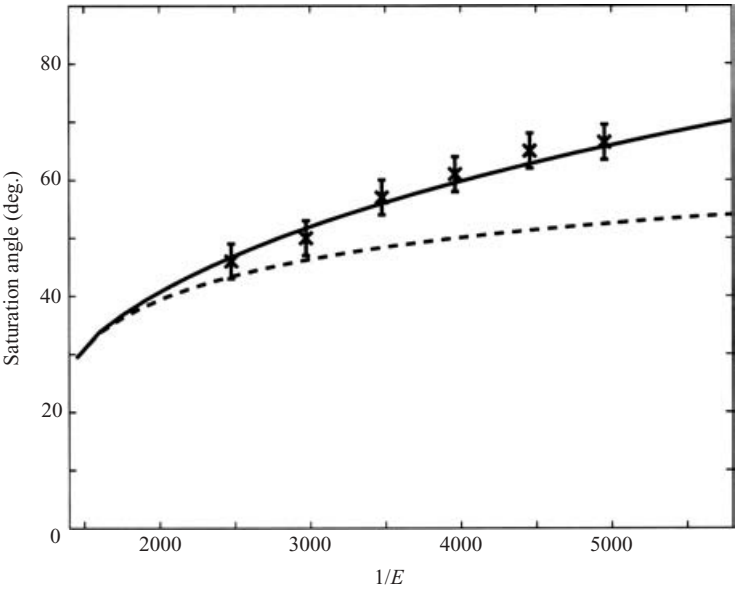


FIGURE 18. Evolution of the saturation angle. ×, experimental data. Nonlinear model (—, maximum angle; - - -, asymptotic angle).

Figure 18 shows that experimental results systematically approach the maxima of the angle obtained by the theory (and not the asymptotic ones) and never come back to the expected ones which are slightly lower. We have no interpretation of this effect, but we suspect that the visualization technique, based on the behaviour of the Kalliroscope flakes, could be at the origin of this discrepancy. For the flow in a deformed rotating cylinder, analysed by Eloy *et al.* (2003), the same discrepancy was observed. However, particle image velocimetry measurements were able to reveal amplitude oscillations before saturation. This might also be the case in the present geometry.

https://doi.org/10.1017/S0022112004008328 Published online by Cambridge University Press

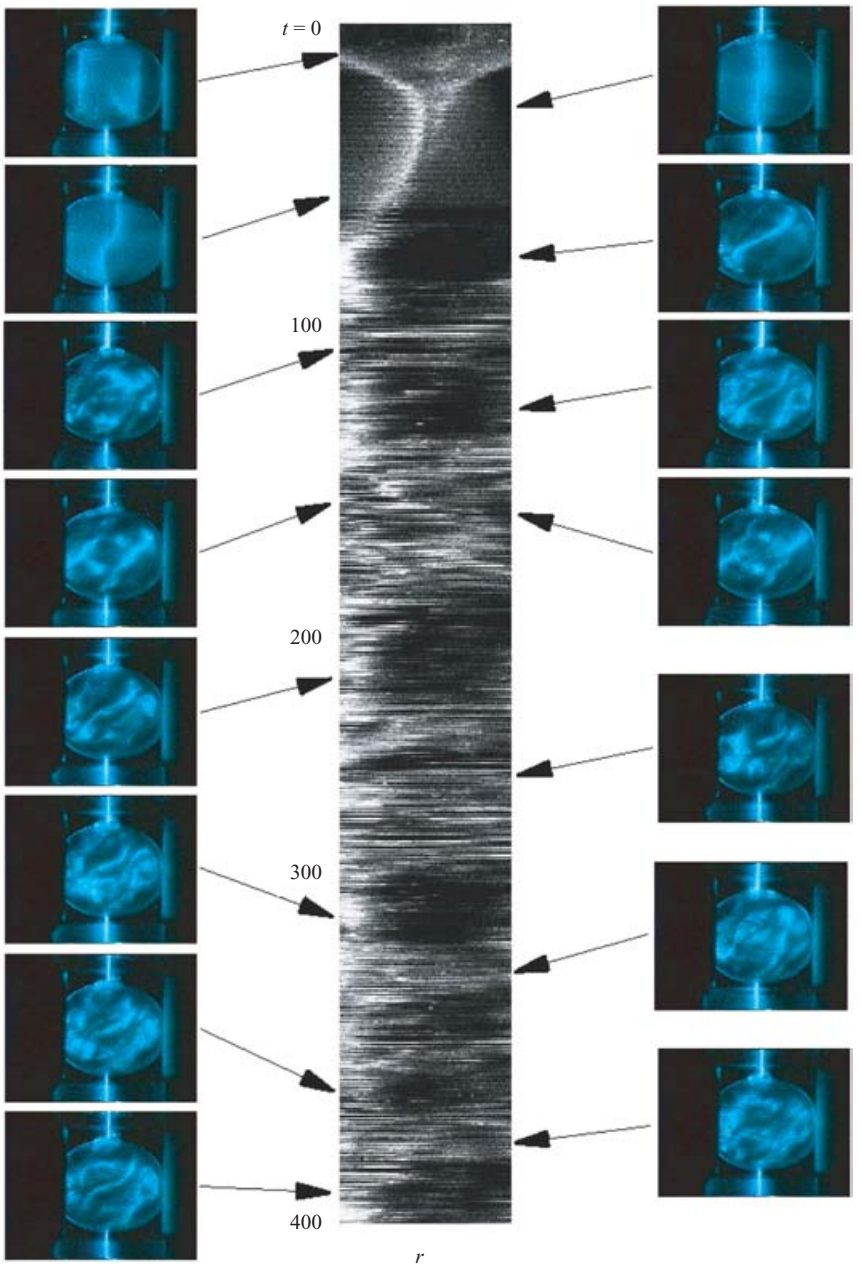


FIGURE 19. Visualizations in the meridional plane of the flow patterns during the spatio-temporal evolution of the intermittent regime ($E = 1.68 \times 10^{-4}$ and $\varepsilon = 0.16$). The bursts observed in the spatio-temporal diagram (centre) correspond to disordered phases during which the S shape of the spin-over mode disappears intermittently (side view).

3.4. *Secondary instability and intermittent regime*

Figure 19 represents a spatio-temporal evolution of the constrained flow for $E = 1.68 \times 10^{-4}$. A series of corresponding images visualize the different states of the flow. The spin-up phase is observed in the first part ($t < 30$). It is immediately

https://doi.org/10.1017/S0022112004008328 Published online by Cambridge University Press

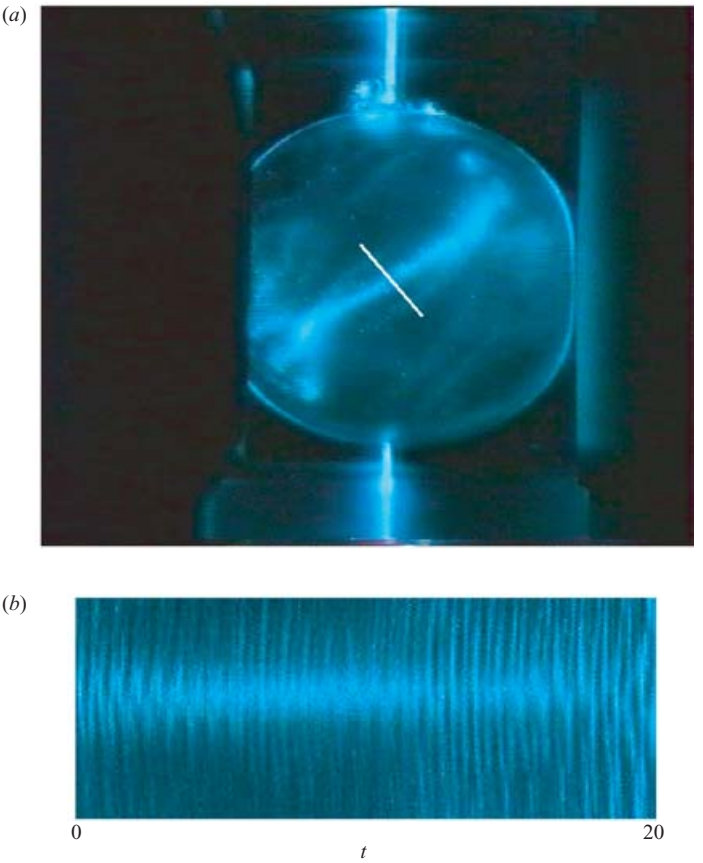


FIGURE 20. Secondary instability of the flow. $E = 1.68 \times 10^{-4}$, $\varepsilon = 0.16$. (*a*) Visualization of the flow, (*b*) spatio-temporal diagram built along the white line of (*a*).

followed by the elliptical instability growth as described in the preceding sections. The spin-over mode is observed to saturate for $70 < t < 80$. During this period, small structures appear between the vortex core and the sphere boundary. Meanwhile, a secondary instability taking the form of a pulsing wave appears in the central part of the S deformed vortex core. Figure 20 presents a visualization of the flow and the corresponding space–time diagram. This diagram was performed on a segment crossing the vortex perpendicularly. It shows the periodic pulsation of this secondary mode. The Fourier spectrum of a time series originating from this diagram shows a frequency peak at 2.13 (figure 21). This value is close to that calculated by Kerswell (1999) in the cylinder (2.27) and observed by Eloy *et al.* (2000). This secondary instability then leads to a destructuring of the flow. The apparently disordered state appears for the first time around $t = 100$. It is followed by a relaminarization process during which the spin-over mode reappears. The flow then enters an intermittent regime with a succession in time of the spin-over mode and chaotic flows. Contrary to the cylindrical case where intermittency has also been observed by Malkus (1989) and Eloy *et al.* (2000), the flow never comes back to the basic rotation around the (*oz*) axis but always relaminarizes toward the spin-over mode. A sequence of this intermittent regime is displayed in the space–time diagram of figure 19 and shows

https://doi.org/10.1017/S0022112004008328 Published online by Cambridge University Press

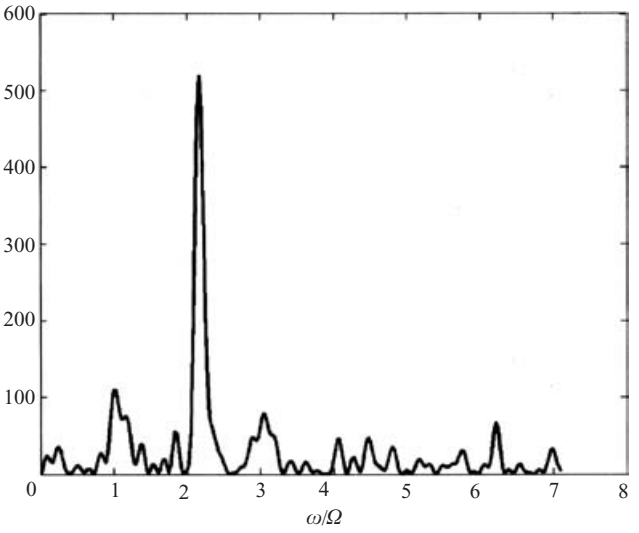


FIGURE 21. Spectrum (arbitrary unit) of the secondary instability of the flow. $E = 1.68 \times 10^{-4}$, $\varepsilon = 0.16$.

several switches between the well-formed spin-over mode and more disordered flows. The different phases have a duration of around one hundred periods of the basic rotation.

4. Conclusion

The elliptical instability of a fluid flow contained in a rotating spheroid has been investigated both theoretically and experimentally. A linear stability analysis has been performed in the limit of weak deformation and small Ekman numbers. A stability diagram showing the characteristics of the most unstable mode has been obtained as a function of the deformation ε and of the Ekman number E. The spin-over mode, which corresponds to a solid-body rotation perpendicular to the main rotation axis, has been found to be the first mode to be destabilized as ε increases or E decreases. It has also been found to be the most unstable mode for the parameters of the experiment. As predicted, our experiment exhibits the structure of the flow pattern and the growth associated with the spin-over mode. The measurement of the experimental growth rate shows that it corresponds to the theoretical predictions especially near the instability threshold. A simplified nonlinear model was also constructed to account for the experimental observations. Without viscosity, the model predicts large periodic heteroclinic oscillations during which the spin-over mode is even able to reverse the sign of the basic flow rotation. This peculiar behaviour has been shown to be suppressed by the addition of the viscous effects associated with the boundary layers. In that case, a saturated regime is reached asymptotically whose characteristics are in agreement with the experimental measurements. Finally, similarly to the observations of the elliptic instability in cylinders, an intermittent regime has also been observed in the sphere. This chaotic regime with cycles a hundred times longer than the basic rotation period seems to be triggered by a secondary instability. The analysis of its characteristics is left for future work.

https://doi.org/10.1017/S0022112004008328 Published online by Cambridge University Press

REFERENCES

Aldridge, A., Seyed-Mahmoud, B., Henderson, G. & Van Wijngaarden, W. 1997 Elliptical instability of the earth's fluid core. *Phys. Earth Planet. Inter.* **103**, 365–374.

Bayly, B. J. 1986 Three-dimensional instability of elliptical flow. *Phys. Rev. Lett.* **57**, 2160–2163.

Biello, J. A., Saldanha, K. I. & Lebovitz, N. R. 2000 Instabilities of exact, time-periodic solutions of the incompressible Euler equations. *J. Fluid Mech.* **404**, 269–287.

Cadot, O., Douady, S. & Couder, Y. 1995 Characterization of the low pressure filaments in three-dimensional turbulent shear flow. *Phys. Fluids* **7**, 630–646.

Eloy, C. 2000 Instabilité multipolaire de tourbillons. PhD thesis, Université Aix-Marseille II.

Eloy, C. & Le Dizès, S. 2001 Stability of the Rankine vortex in a multipolar strain field. *Phys. Fluids* **13**, 660–676.

Eloy, C., Le Gal, P. & Le Dizès, S. 2000 Experimental study of the multipolar vortex instability. *Phys. Rev. Lett.* **85**, 145–166.

Eloy, C., Le Gal, P. & Le Dizès, S. 2003 Elliptic and triangular instabilities in rotating cylinders. *J. Fluid Mech.* **476**, 357–388.

Gledzer, E. B., Dolzhansky, F. V., Obukhov, A. M. & Ponomarev, V. M. 1975 An experimental and theoretical study of the stability of motion of a liquid in an elliptical cylinder. *Izv. Atmos. Ocean. Phys.* **11**, 617–622.

Gledzer, E. B. & Ponomarev, V. M. 1977 Finite dimensional approximation of the motions of an incompressible fluid in an ellipsoidal cavity. *Izv. Atmos. Ocean. Phys.* **13**, 565–569.

Greenspan, H. P. 1968 *The Theory of Rotating Fluids*. Cambridge University Press.

Hollerbach, R. & Kerswell, R. 1995 Oscillatory internal shear layers in rotating and precessing flows. *J. Fluid Mech.* **298**, 327–339.

Hough, S. S. 1895 The oscillations of a rotating ellipsoidal shell containing fluid. *Phil. Trans.* A **186**, 469–506.

Kerswell, R. 1993 The instability of precessing flow. *Geophys. Astrophys. Fluid Dyn.* **72**, 107–144.

Kerswell, R. 1994 Tidal excitation of hydromagnetic waves and their damping in the earth. *J. Fluid Mech.* **274**, 219–241.

Kerswell, R. R. 1999 Secondary instabilities in rapidly rotating fluids: inertial wave breakdown. *J. Fluid Mech.* **382**, 283–306.

Kerswell, R. R. 2002 Elliptical instability. *Annu. Rev. Fluid Mech.* **34**, 83–113.

Kerswell, R. R. & Malkus, W. V. R. 1998 Tidal instability as the source for Io's magnetic signature. *Geophys. Res. Lett.* **25**, 603–606.

Leweke, T. & Williamson, C. H. K. 1998*a* Cooperative elliptic instability of a vortex pair. *J. Fluid Mech.* **360**, 85–119.

Leweke, T. & Williamson, C. H. K. 1998*b* Three-dimensional instabilities in wake transition. *Eur. J Mech.* B/*Fluids* **17**, 571–586.

Malkus, W. 1968 Precession of the earth as the cause of geomagnetism. *Science* **160**, 259–264.

Malkus, W. V. R. 1989 An experimental study of global instabilities due to tidal (elliptical) distortion of a rotating elastic cylinder. *Geophys. Astrophys. Fluid Dyn.* **48**, 123–134.

Meunier, P., Ehrenstein, U., Leweke, T. & Rossi, M. 2002 A merging criterion for two-dimensional co-rotating vortices. *Phys. Fluids* **14**, 2757–2766.

Moore, D. W. & Saffman, P. G. 1975 The instability of a straight vortex filament in a strain field. *Proc. R. Soc. Lond.* A **346**, 413–425.

Noir, J., Jault, D. & Cardin, P. 2000 Numerical study of the motions within a slowly precessing sphere at low Ekman number. *J. Fluid Mech.* **437**, 283–299.

Pierrehumbert, R. T. 1986 Universal short-wave instability of two-dimensional eddies in an inviscid fluid. *Phys. Rev. Lett.* **57**, 2157–2160.

Poincaré, H. 1910 Sur la précession des corps déformables. *Bull. Astron.* **27**, 321–356.

Rieutord, M., Georgeot, B. & Valdettaro, L. 2001 Inertial waves in a rotating spherical shell: attractors and asymptotic spectrum. *J. Fluid Mech.* **435**, 103–144.

Suess, S. T. 1971 Viscous flow in a deformable rotating container. *J. Fluid Mech.* **45**, 189–201.

https://doi.org/10.1017/S0022112004008328 Published online by Cambridge University Press

Tsai, C.-Y. & Widnall, S. E. 1976 The stability of short waves on a straight vortex filament in a weak externally imposed strain field. *J. Fluid Mech.* **73**, 721–733.

Waleffe, F. 1990 On the three-dimensional instability of strained vortices. *Phys. Fluids* A **2**, 76–80.

Widnall, S. E., Bliss, D. & Tsai, C.-Y. 1974 The instability of short waves on a vortex ring. *J. Fluid Mech.* **66**, 35–47.

Zhang, K., Earnshaw, P., Liao, X. & Busse, F. H. 2001 On inertial waves in a rotating fluid sphere. *J. Fluid Mech.* **437**, 103–119.

https://doi.org/10.1017/S0022112004008328 Published online by Cambridge University Press